Disturbance Observer-Based Model Predictive Super-Twisting Control for Soft Open Point

Zhengqi Wang [1] , **Haoyu Zhou** [1,*] **and Hongyu Su** [2]

1 School of Electric Power Engineering, Nanjing Institute of Technology, Nanjing 211167, China; wzqnjit@163.com
2 School of Electrical and Electronic Engineering, Harbin University of Science and Technology, Harbin 150001, China; suzuhys@163.com
* Correspondence: zhy9780@163.com

Abstract: This paper presents a disturbance observer-based model predictive of super-twisting control for Soft Open Point (SOP). First, with the consideration of the disturbances caused by parameter mismatches and unmodelled dynamics, a super-twisting sliding-mode observer (STO) is proposed to observe the disturbances, and the observed disturbances are introduced into the inner-loop as the compensation to improve the anti-disturbance of SOP system. Second, the outer-loop controller is designed by applying the super-twisting sliding-mode control (STC) approach to improve the dynamic performance and robustness. Third, to deal with large current harmonics by traditional model predictive control (MPC), a Three-Vector-based MPC (TV-MPC) is proposed to increase the number of voltage vectors in a sampling time. Finally, it is verified by simulations that the proposed method can reduce current harmonics, DC-side voltage setting time and improve the dynamic performance of SOP system effectively. In case of parameter mismatches, the proposed observer can observe the disturbances correctly to enhance the robustness of the SOP system.

Keywords: Soft Open Point (SOP); model predictive control (MPC); parameter mismatch; super-twisting algorithm; sliding-mode observer

1. Introduction

In recent years, with the popularization and development of renewable energies, increasingly renewable energy sources are connected to electricity distribution networks. However, with the development of renewable energy sources, such problems as voltage instability, bi-directional current and unbalanced power arise in electric energy systems [1,2]. As a new power electronic device, Soft Open Point (SOP) has the advantages of flexible power management of the distribution network, fast response time and various control methods, among others [3]. Therefore, SOP has been widely used in the electricity distribution energy systems.

Two-port SOP can be seen as a back-to-back converter, which consists of two voltage source converters (VSCs) and a DC-side capacitor [4]. The two-port SOP system is depicted in Figure 1. The control proposed for SOP includes traditional proportional-integral (PI) control, droop control and model predictive control (MPC) [5–7]. These methods are widely applied in a SOP system. However, traditional PI control requires many parameters to be designed; when disturbances occur in the SOP system, PI control and droop control are less robust as well. In signal-vector-based MPC, only one voltage vector is applied in the system in a sampling time, which causes large current harmonics and power fluctuations. Therefore, it is necessary to design improved inner and outer loop control to improve the steady state and dynamic state of the SOP system.

In order to solve the problems above, various improved methods are proposed for the inner-loop MPC, such as increasing the number of voltage vectors in a sampling time, dual-vector MPC [8] and three-vector-based MPC [9]; combining other methods, such

as adaptive MPC [10] and fuzzy MPC [11], improving the cost function [12] and delay compensation, and so on [13,14].
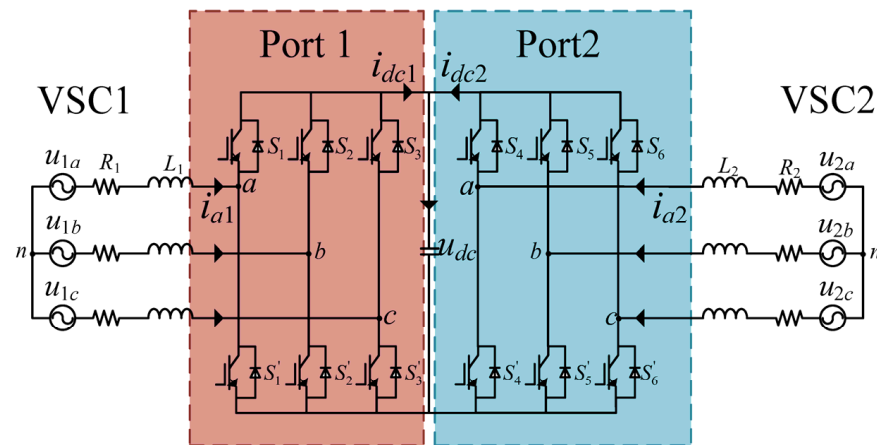

Figure 1. Model of two-port SOP.

Since the MPC of the inner loop is created by accurate model parameters, when disturbances of parameter mismatches and unmodelled dynamics occur in the SOP system in actual operation, predictive errors may occur in the system, due to MPC being sensitive to the parameters, which leads to bad performance of the system [15–17]. Thus, observers are applied in the system to observe the disturbance of the system and considering the disturbance as the compensation of the system to improve the robustness of SOP. Adaptive observers are used in [18] to estimate the capacitors' voltages, which have aa good performance during disturbances. In [19], a Kalman filter is designed to predict the current with reduced noises and estimate the disturbance due to the parameter variation, combined with extended state modeling (ESM). In [20], an extended state observer is applied to enhance the robustness of inductance to cater for the divergence caused by the stator inductance mismatch.

Sliding mode theory is widely used in the design of controllers and observers due to its fast response time and robustness [21–24]. In [25], a sliding-mode controller is designed for a grid-connected NPC inverter to inject a controlled active power while minimizing supply current harmonics, which has the advantages of fast dynamic response and low voltage ripple. Sliding-mode observer is designed for disturbances' estimation in [26], while sliding-mode controllers are designed to solve the consensus problem in second-order nonlinear multi-agent systems. However, due to its own discontinuity, first-order sliding-mode theory has obvious chattering. Super-twisting algorithm (STA), as a second-order sliding-mode theory, can reduce the chattering effectively, while maintaining the advantages of traditional sliding mode [27–32]. In [33], a super-twisting controller is used in permanent linear synchronous motor (PMLSM) to ensure the system convergence and eliminate the chattering phenomenon, thus improving the system's robustness. In [34], a super-twisting nonlinear disturbance observer is proposed, which can estimate the uncertainties and external disturbances. In [35], a super-twisting observer is designed to observe the lump disturbance in the permanent magnet synchronous motor (PMSM) caused by parameter mismatches and consider the disturbances as the compensation to the inner-loop, which improves the robustness of the system.

In this paper, by introducing the theory of the super-twisting algorithm and three-vector-based MPC, a super-twisting sliding-mode controller (STC) and TV-MPC with super-twisting sliding-mode observer (STO) method is proposed to improve the performance of the steady state and dynamic state, and to observe the disturbance correctly under parameter mismatches, the disturbances observed by STO are applied to the TV-MPC as the compensations of the inner-loop. The contributions of this article are listed as follows:

(1)   Compared with traditional outer-loop PI controller, the start-up time and dynamic response of the DC-side voltage are improved by adopting the proposed method;
(2)   Compared with signal-vector method, the current harmonics are improved by applying the TV-MPC method in SOP system;
(3)   Parameter mismatches in the SOP system are considered and compensated for by STO, which improves the adaptation of the SOP system to the disturbances.

The organization of this paper is as follows: Section 2 introduces the model of the two-port SOP system. In Section 3, STO is designed to observe the disturbances. Section 4 designs the outer-loop DC-side voltage STC. Section 5 proposes the TV-MPC method of the SOP system. Section 6 gives the simulation results. Future works are discussed in Section 7. Finally, the conclusions are summarized in Section 8.

2. Mathematical Model of SOP

Since the structure of each port of the SOP is the same, in this paper, one port of the voltage source converter (VSC) is selected to build the mathematical model. Taking VSC1 as an example, the model of one port of the SOP in synchronous rotating frame can be expressed as [36]:

$$\begin{cases} L_1 \frac{di_{d1}}{dt} = -R_1 i_{d1} + \omega L_1 i_{q1} + u_{1d} - S_{d1} u_{dc} \\ L_1 \frac{di_{q1}}{dt} = -R_1 i_{q1} - \omega L_1 i_{d1} + u_{1q} - S_{q1} u_{dc} \end{cases} \tag{1}$$

where i_{d1} and i_{q1} are the *d*- and *q*-axis currents of VSC1, respectively. u_{1d} and u_{1q} are the *d*- and *q*-axis grid voltages of VSC1, respectively. u_{dc} is DC-side voltage; L_1, R_1 and ω are inductance, resistance of VSC1 and voltage angle frequency, respectively. S_{d1} and S_{q1} are the *d*- and *q*-axis modulation switch functions of VSC1, respectively. Similarly, VSC2 has the same mathematical model in synchronous rotating frame.

According to the current direction shown in Figure 1, the relationship between DC-side currents from VSC and from capacitance can be expressed as follows:

$$i_c = C \frac{du_{dc}}{dt} = i_{dc1} + i_{dc2} = \frac{3}{2}(-S_{d1} i_{d1} + S_{q1} i_{q1}) + \frac{3}{2}(-S_{d2} i_{d2} + S_{q2} i_{q2}) \tag{2}$$

where C is the capacitance of DC side, i_{dc1} and i_{dc2} are the DC-side currents from VSC1 and VSC2, respectively. i_c is the DC-side current from capacitance; S_{d2} and S_{q2} are the *d*- and *q*-axis modulation switch functions of VSC2, respectively. i_{d2} and i_{q2} are the *d*- and *q*-axis currents of VSC2, respectively.

By discretizing (1) [37], the discrete model of VSC1 can be obtained as:

$$\begin{cases} i_{d1}(k+1) = (1 - \frac{T_s R_1}{L_1}) i_{d1}(k) + T_s \omega i_{q1}(k) + \frac{T_s}{L_1}(u_{1d}(k) - u_{1Nd}(k)) \\ i_{q1}(k+1) = (1 - \frac{T_s R_1}{L_1}) i_{q1}(k) - T_s \omega i_{d1}(k) + \frac{T_s}{L_1}(u_{1q}(k) - u_{1Nq}(k)) \end{cases} \tag{3}$$

where $i_{d1}(k+1)$ and $i_{q1}(k+1)$ are the predicted *d*- and *q*-axis currents of VSC1 at (k + 1)th instant, respectively. $u_{1Nd}(k)$ and $u_{1Nq}(k)$ are the *d*- and *q*-axis voltages of VSC1, respectively. $i_{d1}(k)$ and $i_{q1}(k)$ are the *d*- and *q*-axis currents of VSC1 at (k)th instant, respectively. $u_{1d}(k)$ and $u_{1q}(k)$ are the *d*- and *q*-axis grid voltages of VSC1 at (k)th instant, respectively. T_s is the sampling time.

Each port of SOP can work in a different mode. DC-side voltage and reactive power are taken as the reference parameters in $U_{dc}Q$ mode, in order to ensure the steadiness of the DC-side voltage, at least one port should work in $U_{dc}Q$ mode in the SOP system. In PQ mode, the active power and reactive power are taken as reference parameters and are most used in the SOP system. In addition, taking the DC-side voltage and frequency as reference parameters the $U_{dc}f$ mode can also be applied in the SOP system when system failure occurs in the system. In this paper, the $U_{dc}Q$ mode is applied in port1 and PQ mode is applied in port2.

3. Design of Super-Twisting Observer under Parameter Mismatch

In the actual operation of the SOP system, both sides work under large current and voltage fluctuations frequently, which makes the parameter changes of resistance and inductances. In this paper, a super-twisting observer (STO) is designed in the inner-loop to observe the disturbances caused by parameter mismatches and unmodelled dynamics, which maintains the strong robustness of the traditional sliding mode observer while suppressinges the high frequency vibration effectively.

Considering the parameter mismatches and unmodelled dynamics, the model of VSC1 can be rewritten as follows:

$$
\begin{cases}
L_1 \frac{\mathrm{d}i_{d1}}{\mathrm{d}t} = -R_1 i_{d1} + \omega L_1 i_{q1} + u_{1d} - (u_{1Nd} - f_{d1}) \\
L_1 \frac{\mathrm{d}i_{q1}}{\mathrm{d}t} = -R_1 i_{q1} - \omega L_1 i_{d1} + u_{1q} - (u_{1Nq} - f_{q1})
\end{cases}
\tag{4}
$$

where u_{1Nd} and u_{1Nq} are the *d*- and *q*-axis voltages of VSC1, respectively. f_{d1} and f_{q1} are the *d*- and *q*-axis disturbances of VSC1 caused by parameter mismatches and unmodelled dynamics, respectively. Due to disturbances' change slowly in steady-state, f_{d1} and f_{q1} can be written as:

$$
\begin{cases}
f_{d1} = -\frac{L_1(L_{10}\Delta R_1 - R_{10}\Delta L_1)}{(L_{10}(L_{10}+\Delta L_1))} i_{d1} - \frac{L_1 \Delta L_1}{(L_{10}(L_{10}+\Delta L_1))}(u_{1Nd} - u_{1d}) + \varepsilon_{d1} \\
f_{q1} = -\frac{L_1(L_{10}\Delta R_1 - R_{10}\Delta L_1)}{(L_{10}(L_{10}+\Delta L_1))} i_{q1} - \frac{L_1 \Delta L_1}{(L_{10}(L_{10}+\Delta L_1))}(u_{1Nq} - u_{1q}) + \varepsilon_{q1}
\end{cases}
\tag{5}
$$

where ε_{d1} and ε_{q1} are the *d*- and *q*-axis unmodelled dynamics disturbances of VSC1; L_{10} and R_{10} are offline parameters of inductance and resistance of VSC1, respectively; variable matrix x_1 is defined as:

$$
\frac{f_1}{L_1} = x_1
\tag{6}
$$

where $f_1 = [f_{d1}, f_{q1}]^T$, $x_1 = [x_{d1}, x_{q1}]^T$.

Errors of inductance parameters and resistance parameters ΔL_1 and ΔR_1 are uncertain and bounded, the unmodelled dynamics disturbance ε_{d1} and ε_{d1} are bounded, which can be written as:

$$
\begin{cases}
|\Delta L_1| \leq \varphi_L \\
|\Delta R_1| \leq \varphi_R \\
|\varepsilon_{d1}| \leq \varphi_{\varepsilon d1} \\
|\varepsilon_{q1}| \leq \varphi_{\varepsilon q1}
\end{cases}
\tag{7}
$$

where φ_L, φ_R and $\varphi_{\varepsilon d1}$ and $\varphi_{\varepsilon q1}$ are the known positive constants.

Due to the assumption above, the disturbance f_{d1} and f_{q1} are bounded and can be assumed as:

$$
\begin{cases}
|f_{d1}| \leq \varphi_{d1} \\
|f_{q1}| \leq \varphi_{q1} \\
\varphi_{d1} \leq \varphi_1 \\
\varphi_{q1} \leq \varphi_1
\end{cases}
\tag{8}
$$

where φ_{d1}, φ_{q1} and φ_1 are known positive constants.

The sliding manifold is designed as:

$$
\begin{cases}
s_{d1} = \hat{i}_{d1} - i_{d1} \\
s_{q1} = \hat{i}_{q1} - i_{q1}
\end{cases}
\tag{9}
$$

where $\hat{i}_{d1}$ and $\hat{i}_{q1}$ are the *d*- and *q*-axis estimated current of VSC1.

Proposition 1. *If the sliding manifold is chosen as (9), the super-twisting observer can be designed as follows:*

$$
\begin{cases}
\frac{d\hat{i}_{d1}}{dt} = \frac{u_{1d}}{L_1} - \frac{R_1}{L_1}\hat{i}_{d1} + \omega\hat{i}_{q1} - \frac{u_{1Nd}}{L_1} + d_d \\
\frac{d\hat{i}_{q1}}{dt} = \frac{u_{1q}}{L_1} - \frac{R_1}{L_1}\hat{i}_{q1} - \omega\hat{i}_{d1} - \frac{u_{1Nq}}{L_1} + d_q \\
d_d = -\alpha_1|s_{d1}|^{\frac{1}{2}}\mathrm{sgn}(s_{d1}) + \hat{x}_{d1} \\
d_q = -\alpha_1|s_{q1}|^{\frac{1}{2}}\mathrm{sgn}(s_{q1}) + \hat{x}_{q1} \\
\hat{x}_{d1} = -\int \beta_1\mathrm{sgn}(s_{d1})dt \\
\hat{x}_{q1} = -\int \beta_1\mathrm{sgn}(s_{q1})dt
\end{cases}
\tag{10}
$$

where d_d and d_q are the d- and q-axis error dynamics of the disturbance; α_1 and β_1 are the designed gains of observer.

The estimated disturbance $\hat{f}_1$ can be expressed as follows according to (6):

$$
\hat{f}_1 = L_1\hat{x}_1
\tag{11}
$$

Proof of Proposition 1. Taking VSC1 as analysis, the Lyapunov function is designed as [38,39]:

$$
V(\gamma) = \gamma^T \boldsymbol{M} \gamma
\tag{12}
$$

where $\gamma^T = \begin{bmatrix} |s_1|^{\frac{1}{2}}\mathrm{sgn}(s_1) & \int \beta_1\mathrm{sgn}(s_1)dt \end{bmatrix}$, $\boldsymbol{M} = \frac{1}{2}\begin{bmatrix} 4\beta_1 + \alpha_1^2 & -\alpha_1 \\ -\alpha_1 & 2 \end{bmatrix}$, $s_1 = [s_{d1}, s_{q1}]^T$.

The time derivative of (12) is expressed as:

$$
\dot{V}(\gamma) = -|s_1|^{-\frac{1}{2}}\gamma^T \boldsymbol{M}_1 \gamma + f_1|s_1|^{-\frac{1}{2}}\boldsymbol{M}_2\gamma
\tag{13}
$$

where $\boldsymbol{M}_1 = \frac{\alpha_1}{2}\begin{bmatrix} 2\beta_1 + \alpha_1^2 & -\alpha_1 \\ -\alpha_1 & 1 \end{bmatrix}$, $\boldsymbol{M}_2 = \begin{bmatrix} (2\beta_1 + \frac{\alpha_1^2}{2}) & \frac{-\alpha_1}{2} \end{bmatrix}$.

Using the bound of disturbance f_1 (8), bound of $\dot{V}(\gamma)$ can be obtained as follows:

$$
\dot{V}(\gamma) \le -|S_1|^{-\frac{1}{2}}\gamma^T \boldsymbol{M}_3 \gamma
\tag{14}
$$

where $\boldsymbol{M}_3 = \frac{\alpha_1}{2}\begin{bmatrix} 2\alpha_1 + \alpha_1^2 - (\frac{4\beta_1}{\alpha_1} + \alpha_1)\varphi_1 & -(\alpha_1 + 2\varphi_1) \\ -(\alpha_1 + 2\varphi_1) & 1 \end{bmatrix}$.

$\dot{V}(\gamma)$ is negative, and the system is strongly globally asymptotically stable when α_1 and β_1 are satisfied as follows:

$$
\begin{cases}
\alpha_1 > 2\varphi_1 \\
\beta_1 > \alpha_1\frac{5\alpha_1\varphi_1 + 4\varphi_1^2}{2(\alpha_1 - 2\varphi_1)}
\end{cases}
\tag{15}
$$

Proofs of VSC2 are similar to the VSC1 side. The proof of the observer stability is completed, which means the values of estimated current approach the values of system current in finite time. □

Figure 2 illustrates the block diagram of STO. The initial values of the integrators are set as 0.

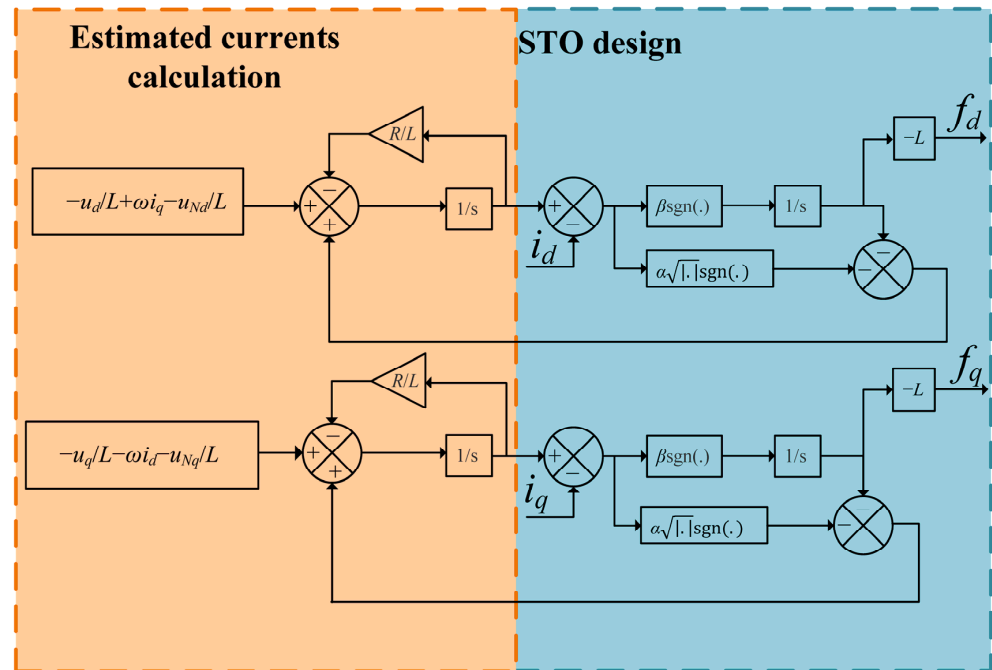**Figure 2.** Block diagram of STO.

4. Design of Outer-Loop Super-Twisting Controller Design

In this paper, port1 is operated in $U_{dc}Q$ mode, which keeps the stability of the DC-side voltage. However, in the traditional outer-loop PI controller, the constant parameters of controller may lead to poor dynamic performance when the parameters of the system are changed. As a second-order sliding mode controller, the super-twisting controller (STC) can effectively suppress the chattering of the first-order sliding mode controller while having a better dynamic performance compared with the PI controller. An outer-loop super-twisting voltage controller is designed in this section.

The outer-loop system of VSC1 is composed of the DC voltage loop, the sliding manifold is designed as:

$$S = u_{dcref} - u_{dc} \tag{16}$$

Uncertain disturbance δ is unknown, but can be assumed to be bounded as follows:

$$|\delta| \leq \rho \tag{17}$$

where ρ is a known positive constant.

Proposition 2. *In order to track the reference DC-side voltage, according to the theory of super-twisting algorithm (STA), when u_{dc} is the system-state variable, STA of u_{dc} can be described as:*

$$\frac{\mathrm{d}u_{dc}}{\mathrm{d}t} = -k_1|S|^{\frac{1}{2}}\mathrm{sgn}(S) - \int k_2\mathrm{sgn}(S) + \delta \tag{18}$$

where $k_1 > 0$ and $k_2 > 0$ are the controller gains.

When the grid voltages are three-phase balanced and the system is stable, the state of the *d*- and *q*-axis currents of AC side i_d and i_q can be written as:

$$\begin{cases} i_q = 0 \\ \frac{\mathrm{d}i_d}{\mathrm{d}t} = 0 \end{cases} \tag{19}$$

where $i_q = [i_{q1}, i_{q2}]^T$, $i_d = [i_{d1}, i_{d2}]^T$.

Substituting (19) into (2) and (1), which can be rewritten as:

$$C\frac{\mathrm{d}u_{dc}}{\mathrm{d}t} = -\frac{3}{2}i_{d1}s_{d1} - \frac{3}{2}i_{d2}s_{d2} \tag{20}$$

$$\begin{cases} S_{d1} = \frac{u_{1d}-R_1 i_{d1}}{u_{dc}} \\ S_{d2} = \frac{u_{2d}-R_2 i_{d2}}{u_{dc}} \end{cases} \tag{21}$$

where u_{2d} is the *d*-axis grid voltage of VSC2.

Substituting (21) into (20), i_{d1} can be rewritten as:

$$i_{d1} = \frac{-\frac{2}{3}Cu_{dc}\frac{\mathrm{d}u_{dc}}{\mathrm{d}_t} - i_{d2}(u_{2d} - R_2 i_{d2})}{u_{1d} - R_1 i_{d1}} \tag{22}$$

when the system is stable, $i_{d1} = i_{d1ref}$, (22) can be rewritten as:

$$i_{d1ref} = \frac{-\frac{2}{3}Cu_{dc}\frac{\mathrm{d}u_{dc}}{\mathrm{d}t} - i_{d2}(u_{2d} - R_2 i_{d2})}{u_{1d} - R_1 i_{d1}} \tag{23}$$

Substituting (18) into (23), the output of the controller id1ref can be written as:

$$i_{d1ref} = \frac{\frac{2}{3}Cu_{dc}(k_1|S|^{\frac{1}{2}}\mathrm{sgn}(S) + \int k_2\mathrm{sgn}(S)\mathrm{d}t) - i_{d2}(u_{2d} - R_2 i_{d2})}{u_{1d} - R_1 i_{d1}} \tag{24}$$

Proof of Proposition 2. The Lyapunov function is designed as:

$$V(\zeta) = \zeta^T P \zeta \tag{25}$$

where $\zeta^T = \begin{bmatrix} |S|^{\frac{1}{2}}\mathrm{sgn}(S) & \int k_2\mathrm{sgn}(S)\mathrm{d}t \end{bmatrix}$, $P = \frac{1}{2}\begin{bmatrix} 4k_2 + k_1^2 & -k_1 \\ -k_1 & 2 \end{bmatrix}$.

The time derivative of (25) is expressed as:

$$\dot{V}(\zeta) = -|S|^{-\frac{1}{2}}\zeta^T P_1 \zeta + \delta|S|^{-\frac{1}{2}}P_2\zeta \tag{26}$$

where $P_1 = \frac{k_1}{2}\begin{bmatrix} 2k_2 + k_1^2 & -k_1 \\ -k_1 & 1 \end{bmatrix}$, $P_2 = \begin{bmatrix} (2k_2 + \frac{k_1^2}{2}) & \frac{-k_1}{2} \end{bmatrix}$.

Using the bound of disturbance δ (17), the bound of $\dot{V}(\zeta)$ can be obtained as follows:

$$\dot{V}(\zeta) \le -|S|^{-\frac{1}{2}}\zeta^T P_3 \zeta \tag{27}$$

where $P_3 = \frac{k_1}{2}\begin{bmatrix} 2k_1 + k_1^2 - (\frac{4k_2}{k_1} + k_1)\rho & -(k_1 + 2\rho) \\ -(k_1 + 2\rho) & 1 \end{bmatrix}$.

$\dot{V}(\zeta)$ is negative and the system is strongly globally asymptotically stable when k_1 and k_2 are satisfied as follows:

$$\begin{cases} k_1 > 2\rho \\ k_2 > k_1\frac{5k_1\rho+4\rho^2}{2(k_1-2\rho)} \end{cases} \tag{28}$$

When k_1 and k_2 are satisfied in the equation above, the error dynamic of DC-side voltage approaches the ideal sliding manifold $S = 0$ in finite time. The proof is completed. $\square$
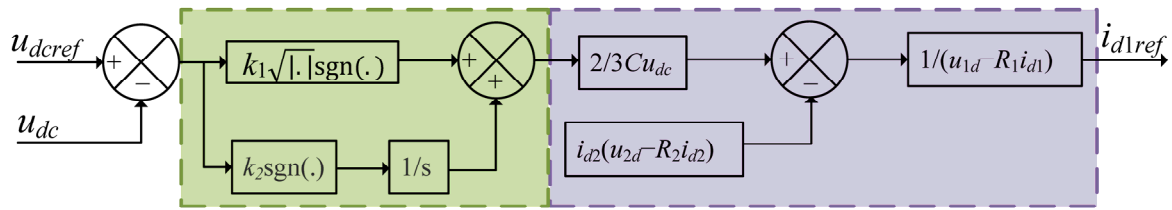
Figure 3 shows the block diagram of outer-loop STC.

Figure 3. Block diagram of outer-loop STC.

5. Inner-Loop TV-MPC for SOP

5.1. Traditional MPC Method

In the SOP system consisting of two-level VSC, the switch states can be divided into six active voltage vectors (V1, V2, V3, V4, V5, V6) and two zero vectors (V0, V7), as shown in Figure 4. As shown in Figure 1, '1' in Figure 4 means the switch S_x is on and S'_x is off, while '0' means the switch S_x is off and S'_x is on (x = 1, 2, 3, 4, 5, 6).
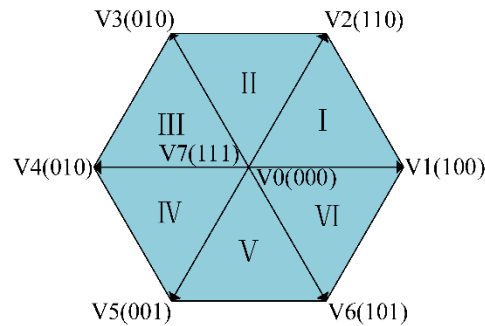

Figure 4. Voltage vector of VSC.

Port1 is operated in $U_{dc}Q$ mode to ensure the stability of the DC-side voltage. In the traditional MPC method, the PI controller is used in the outer-loop subsystem to output *d*-axis reference current i_{d1ref}, which can be expressed as:

$$i_{d1ref} = k_p(u_{dcref} - u_{dc}) + k_i \int (u_{dcref} - u_{dc})\mathrm{d}t \tag{29}$$

where k_p and k_i are the proportional and integral coefficients of PI controller, respectively. u_{dcref} is the reference voltage of the DC side.

The PQ mode is used in Port2. With a stable grid voltage, a given reference current is equivalent to a given reference power, which can transform the PQ mode control into a problem of tracking the reference current.

Taking VSC1 for analysis, since two zero vectors V0 and V7 obtain the same voltage vector, in traditional MPC, seven voltage vectors are substituted into (3) to calculate the corresponding predicted currents, and each predicted current is substituted into the cost function, the voltage vector with the smallest cost function value can be selected as the optimal voltage vector and applied to the switch in the next sampling time. The cost function can be designed as:

$$f = \left| i_{d1ref} - i_{d1}(\mathrm{k}+1) \right| + \left| i_{q1ref} - i_{q1}(\mathrm{k}+1) \right| \tag{30}$$

where i_{q1ref} is the *q*-axis current reference value of VSC1.

Similarly, VSC2 with given reference current, cost function values can be calculated and the optimal voltage vector will be applied to the switch in the next sampling time.

5.2. TV-MPC Method

In the traditional MPC method, only one voltage vector can be used in a sampling time and seven times of cost function calculations are required at both port, which leads

to large current harmonics and control delays. Therefore, using the principle of deadbeat control, a low-complexity TV-MPC method is proposed. By calculating the predicted value of the reference voltage of VSC at the next sampling time, using Table 1 to judge the sector and selecting a zero vector and two active voltage vectors in this sector as the vector combination. The vector combination is applied to the VSC at the next sampling time.

Table 1. Voltage vector combination selection.

Sector	Voltage Vector Combination
I	V1, V2, V0 or V7
II	V2, V3, V0 or V7
III	V3, V4, V0 or V7
IV	V4, V5, V0 or V7
V	V5, V6, V0 or V7
VI	V6, V1, V0 or V7

Taking VSC1 as the example, in the principle of deadbeat control, assuming the predicted currents at (k + 1)th instant as follows:

$$\begin{cases} i_{d1ref} = i_{d1}(k+1) \\ i_{q1ref} = i_{q1}(k+1) \end{cases} \tag{31}$$

Substituting (31) into (3), the reference voltages of VSC1 u_{1Ndref} and u_{1Nqref} can be written as:

$$\begin{cases} u_{1Ndref} = \frac{L_1}{T_s}(i_{d1}(k) - i_{d1ref}) - R_1 i_{d1}(k) + L_1 \omega i_{q1}(k) + u_{1d}(k) \\ u_{1Nqref} = \frac{L_1}{T_s}(i_{q1}(k) - i_{q1ref}) - R_1 i_{q1}(k) - L_1 \omega i_{d1}(k) + u_{1q}(k) \end{cases} \tag{32}$$

According to u_{1Ndref} and u_{1Nqref}, the sector can be determined. The optimal vector combination u_{1opt}, u_{2opt} and u_{0opt} include two active voltage vectors and one zero vector. For the selected optimal vector combination, the action time of each vector in a sampling time needs to be calculated. The principle of modulation MPC is applied, assuming the voltage vector action time is inversely proportional to the cost function value. The action time of voltage vectors t_1, t_2 and t_0 can be calculated as:

$$\begin{cases} t_1 = \frac{n}{f_1} T_s \\ t_2 = \frac{n}{f_2} T_s \\ t_0 = \frac{n}{f_0} T_s \\ n = \frac{1}{f_1^{-1} + f_2^{-1} + f_0^{-1}} \end{cases} \tag{33}$$

where f_1, f_2 and f_0 are the values of cost function (30) corresponding to u_{1opt}, u_{2opt} and u_{0opt}, respectively. In this section, i_{d1ref} is calculated by STC (24).

VSC2 is similar to VSC1, the optimal voltage vectors with the corresponding action times are output to the switches at the next sampling time, which will control the whole SOP system.

5.3. TV-MPC with STO

After adding the disturbance observed by STO, (32) can be rewritten as follows:

$$\begin{cases} u_{1Ndref} = \frac{L_1}{T_s}(i_{d1}(k) - i_{d1ref}) - R_1 i_{d1}(k) + L_1 \omega i_{q1}(k) + u_{1d}(k) + \hat{f}_{d1} \\ u_{1Nqref} = \frac{L_1}{T_s}(i_{q1}(k) - i_{q1ref}) - R_1 i_{q1}(k) - L_1 \omega i_{d1}(k) + u_{1q}(k) + \hat{f}_{q1} \end{cases} \tag{34}$$

The new voltage combination can be selected by the reference voltage u_{d1ref} and u_{q1ref}. By the new voltage combination, the values of cost function and action time of each vector can be recalculated.

After adding the disturbance, (3) can be rewritten as:

$$
\begin{cases}
i_{d1}(k+1) = (1 - \frac{T_s R_1}{L_1})i_{d1}(k) + T_s \omega i_{q1}(k) + \frac{T_s}{L_1}(u_{1d}(k) - u_{1Nd}(k) + \hat{f}_{d1}) \\
i_{q1}(k+1) = (1 - \frac{T_s R_1}{L_1})i_{q1}(k) - T_s \omega i_{d1}(k) + \frac{T_s}{L_1}(u_{1q}(k) - u_{1Nq}(k) + \hat{f}_{q1})
\end{cases}
\tag{35}
$$

After substituting the rewritten predicted currents of (k + 1)th instant by new vector combinations chosen by (34) into (30) the values of the cost function can be calculated. Action times of each voltage vectors t_1, t_2 and t_0 can be calculated by (33).

VSC2 is similar to VSC1, new voltage combinations and action times are output to each side of switch and control the whole system of SOP.

Figure 5 is the block diagram of the STC and TV-MPC with STO for SOP.
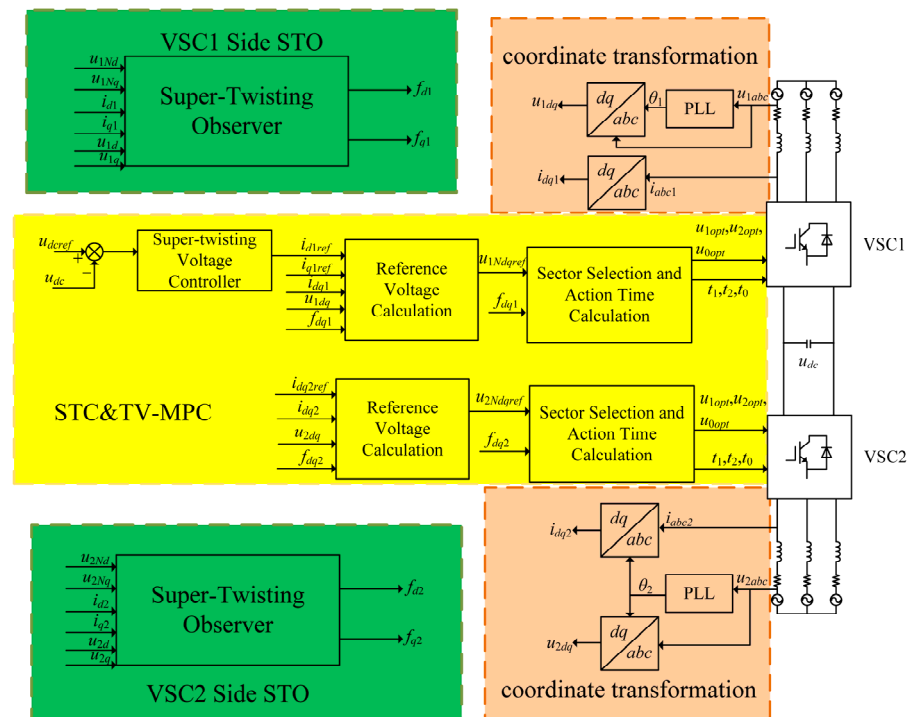

Figure 5. Block diagram of the proposed control scheme of SOP.

6. Simulations

In this paper, traditional MPC, TV-MPC and TV-MPC with STC were designed to demonstrate the effectiveness of the proposed method and were simulated in MAT-LAB/Simulation. TV-MPC and STO with STC was designed when parameter mismatches occurred in the SOP system. Table 2 lists the parameters of the SOP system.

Table 2. Parameters of SOP.

Name	Symbol	Value
VSC1 grid voltage	u_1	220 V
VSC2 grid voltage	u_2	220 V
VSC1 resistance	R_1	0.03 Ω
VSC2 resistance	R_2	0.03 Ω
VSC1 inductance	L_1	3 mH
VSC2 inductance	L_2	3 mH
DC-side capacitance	C	5000 μF f
Sampling time	T_s	1×10^{-6} s

6.1. Current Pefromance of Steady-State

The proposed current of VSC2 side is set as -40 A in simulations. Outer-loop controller parameters are listed in Table 3. Steady-state currents of PI and MPC, PI and TV-MPC and STC and TV-MPC are shown in Figure 6.

It can be seen that in VSC1 side, the total harmonic distortions (THDs) of a-phase of PI and MPC, PI and TV-MPC and STC and TV-MPC are 1.07%, 0.43% and 0.58%, respectively. While on VSC2 side, the THD of a-phase of PI and MPC, PI and TV-MPC and STC and TV-MPC are 1.06%, 0.43% and 0.44%, respectively. Compared with PI and MPC, it is obvious that PI and TV-MPC has a better steady-state current performance and reduces the current ripple of each side. Current performances of STC and TV-MPC are similar to PI and TV-MPC, maintaining the low current ripple of the system.

Table 3. Controller parameters.

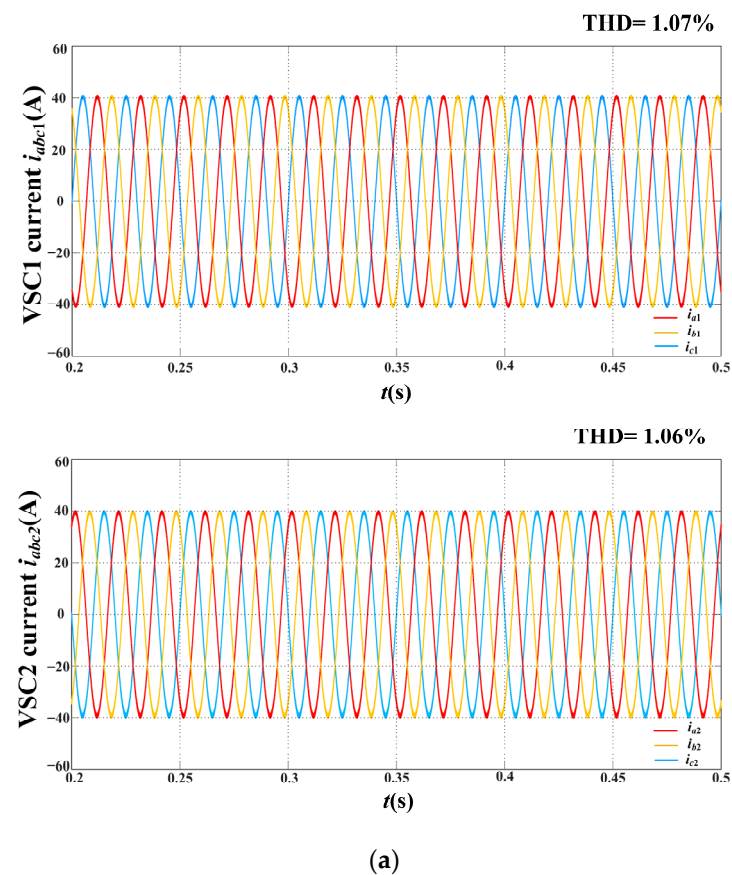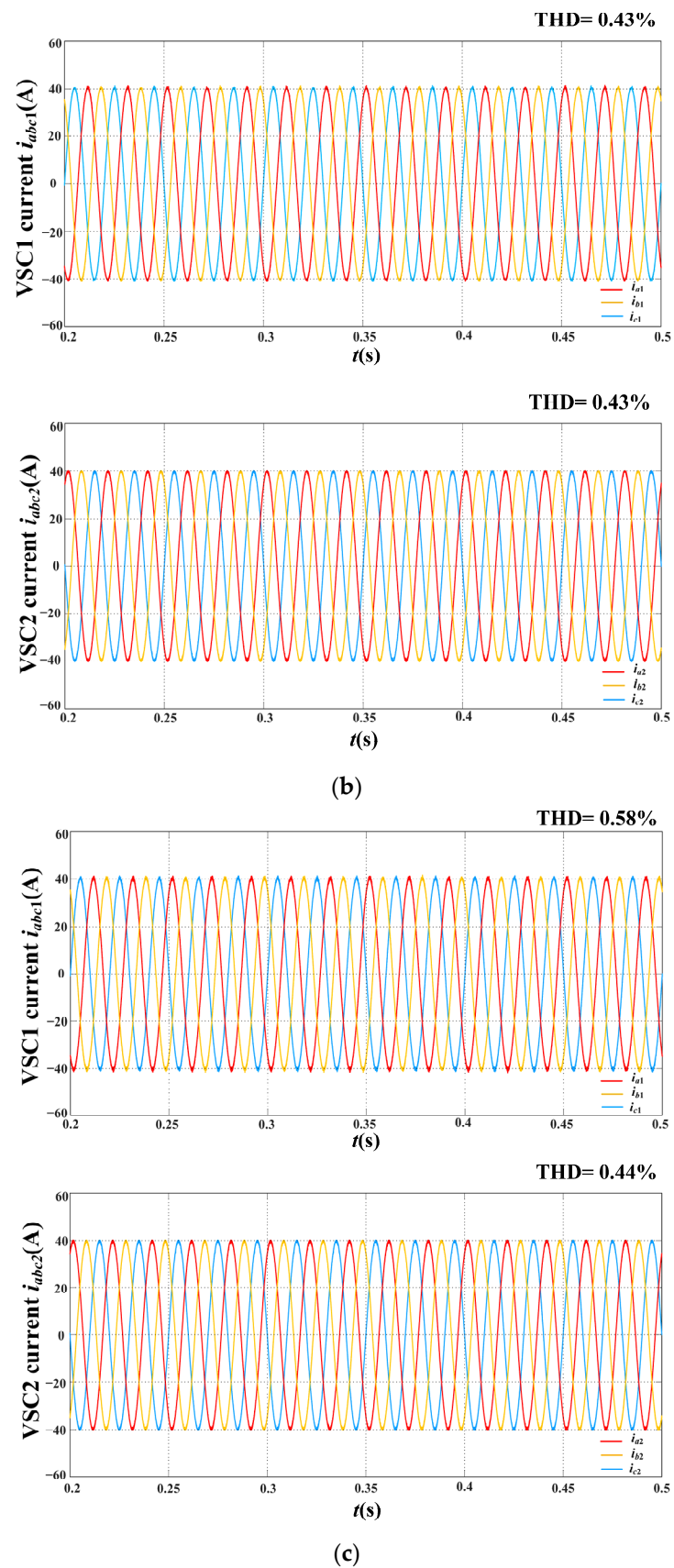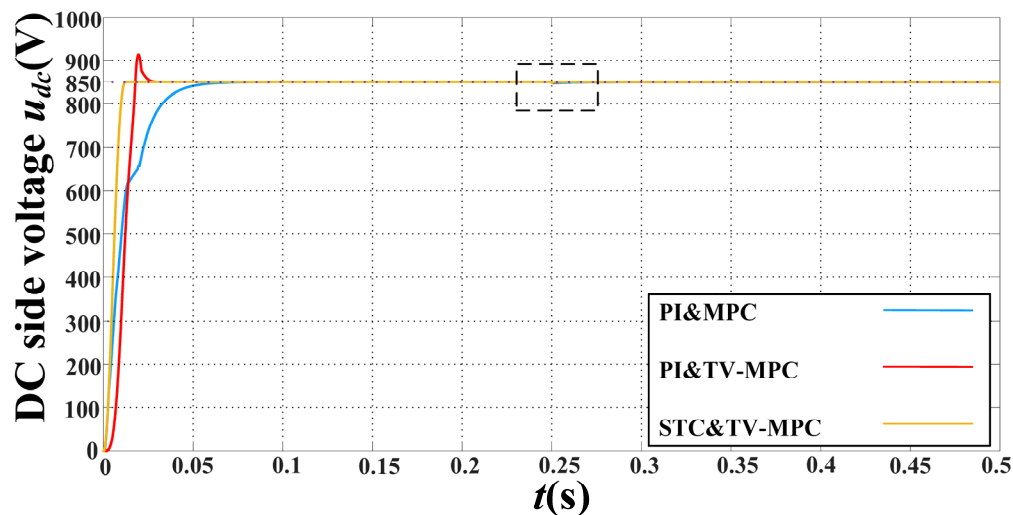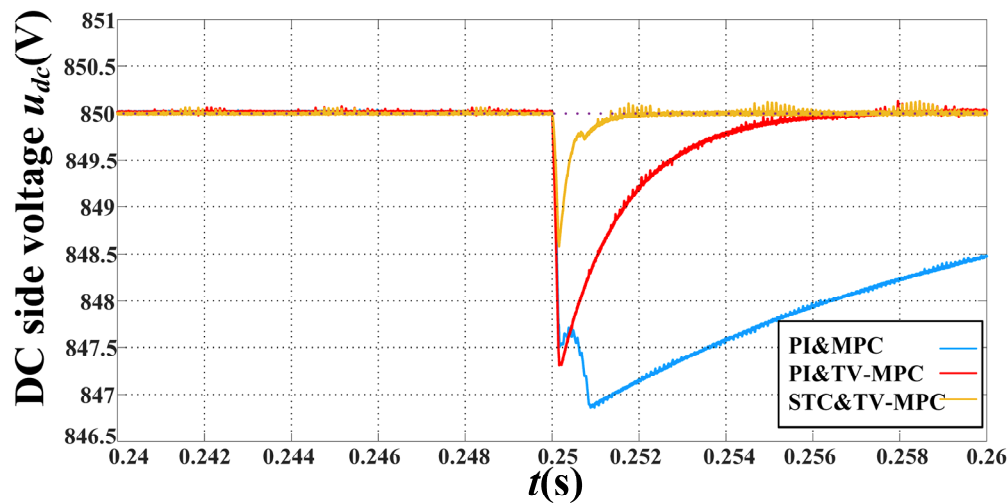| Method	Outer-Loop Controller Parameters
PI and MPC	$k_p = 3.5, k_i = 4.125$
PI and TV-MPC	$k_p = 3.5, k_i = 4.125$
STC and TV-MPC	$k_1 = 150, k_2 = 3000$

(a)

Figure 6. *Cont.*

Figure 6. (**a**) Current waveform and THD of PI and MPC; (**b**) Current waveform and THD of PI and TV-MPC; (**c**) Current waveform and THD of STC and TV-MPC.

6.2. DC Voltage Performance

Regulating the proposed DC-side voltage u_{dcref} at 850 V, in order to verify the effectiveness of STC+TV-MPC in start-up response performance and dynamic state performance, the reference current of VSC2 side is changed from 40 A to 80 A at 0.25 s. As is shown in Figure 7a, the time used to track the proposed DC voltage under PI and MPC, PI and TV-MPC and STC and TV-MPC are 0.108 s, 0.029 s and 0.016 s, respectively. It can be seen that STC and TV-MPC track the proposed DC voltage faster than PI and MPC and PI and TV-MPC without overshoot, which has a better start-up response performance.

(a)

(b)

Figure 7. (**a**) DC-side voltage waveform of PI and MPC, PI and TV-MPC and STC and TV-MPC; (**b**) Detailed view of (**a**) in dynamic state.

Changes of the DC-side voltage in dynamic state are shown in Figure 7b. It can be seen that the time used to recover the proposed DC-side voltage and voltage drops of STC and TV-MPC is much less than PI and MPC and PI and TV-MPC.

As a result, it can be seen that STC and TV-MPC has better performance in start-up response and current change response.

6.3. STC and TV-MPC with STO under Parameter Mismatches

In order to prove the effectiveness of STC and TV-MPC with STO, the SOP system under parameter mismatches is simulated in this section. STO and STC parameters are listed in Table 4.

Table 4. STO and STC parameters.

k_1	k_2	α_1	β_1	α_2	β_2
100	200	50,000	1,500,000	50,000	1,500,000

The proposed current of VSC2 side is set as 40 A, when parameter mismatches have not occurred in the SOP system, Figure 8a shows the d-axis currents of SOP system i_{d1}, i_{d2}, i_{d1ref} and i_{d2ref}. Figure 8b shows the q-axis currents of SOP system i_{q1}, i_{q2}, i_{q1ref} and i_{q2ref}. The disturbances f_{d1}, f_{q1}, f_{d2} and f_{q2} estimated by STO are shown in Figure 8c. It can be seen that when parameter mismatches have not occurred in SOP system, i_{d1}, i_{q1}, i_{d2} and i_{q2} can track the reference currents correctly and the disturbances estimated by STO are small.
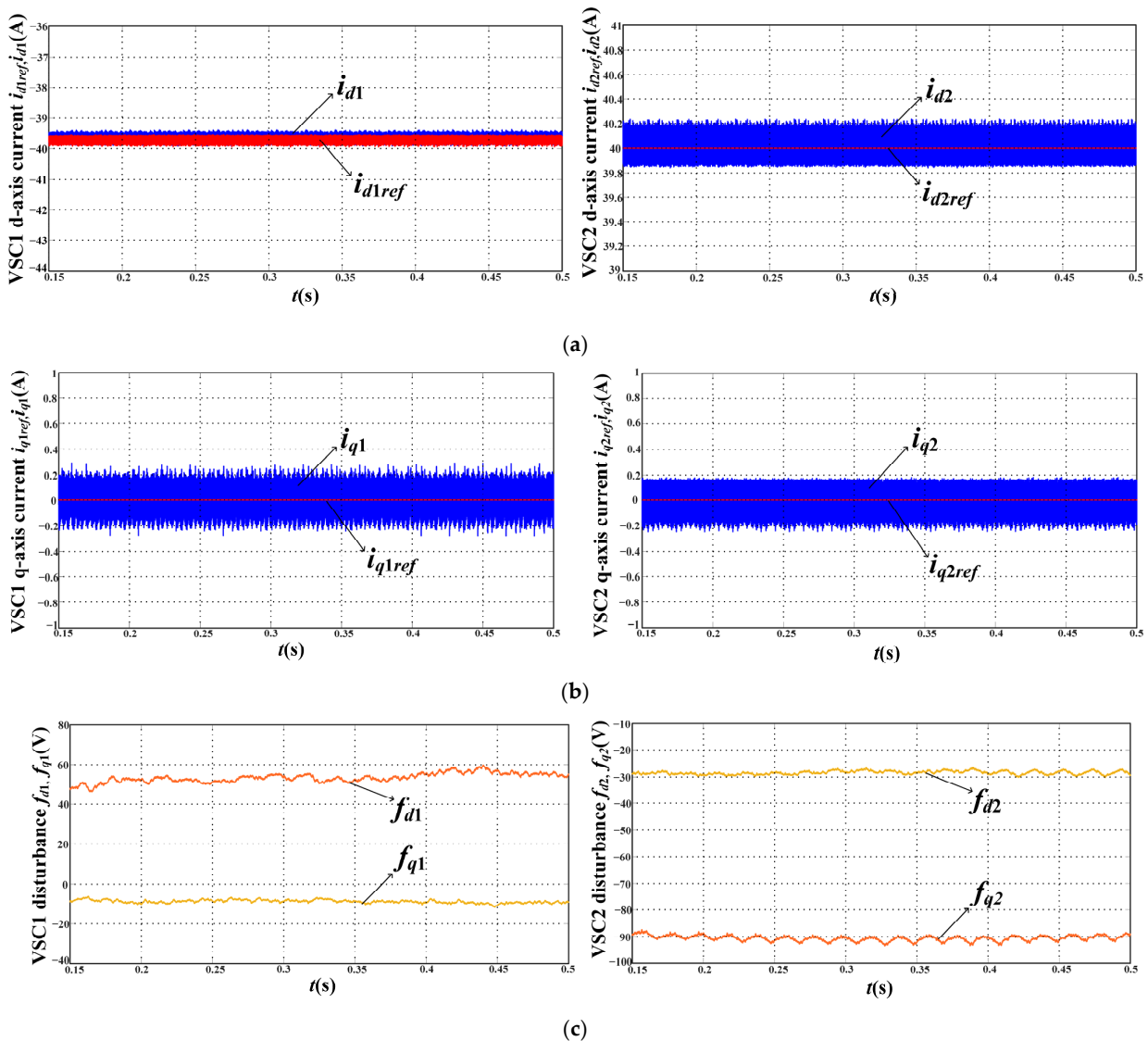

(a)

(b)

(c)

Figure 8. (**a**) d-axis currents of SOP with no parameter mismatches; (**b**) q-axis currents of SOP with no parameter mismatches; (**c**) Disturbances observed by STO with no parameter mismatches.

When inductance mismatches have occurred in the SOP system, STO can observe the disturbances caused by inductance mismatches. The SOP system starts at 0 s and ends at 0.8 s, while the observers are applied to the system at 0.4 s. When system inductances become $5L_1$ and $5L_2$, as shown in Figure 9a, inductances' mismatches influence the d-axis currents obviously, Figure 9b shows the q-axis currents, when observers are applied to the system at 0.4 s, currents can track the reference currents correctly. Figure 9c shows the disturbances estimated by STO, it can be seen that after a short time, the estimated disturbances can be stabilized. When system inductances become $0.3L_1$ and $0.3L_2$, Figure 10a–c present the d-axis current, q-axis current and disturbances estimated by STO, respectively, it can be seen the STO can also estimate the disturbances correctly. These results verify the effectiveness of proposed STO.
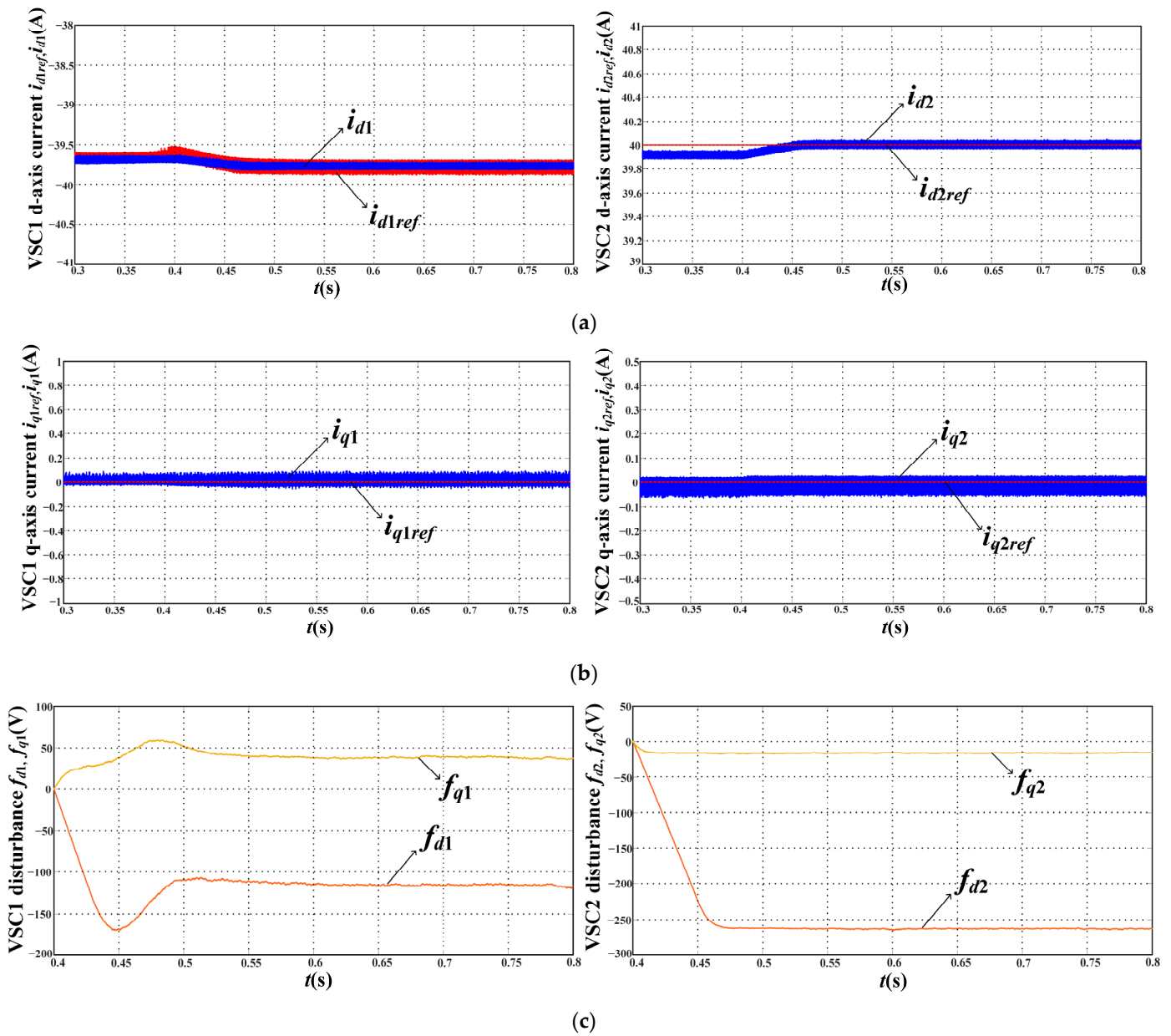

(a)

(b)

(c)

Figure 9. (**a**) d-axis currents of SOP with $5L_1$ and $5L_2$; (**b**) q-axis currents of SOP with $5L_1$ and $5L_2$; (**c**) disturbances observed by STO with $5L_1$ and $5L_2$.
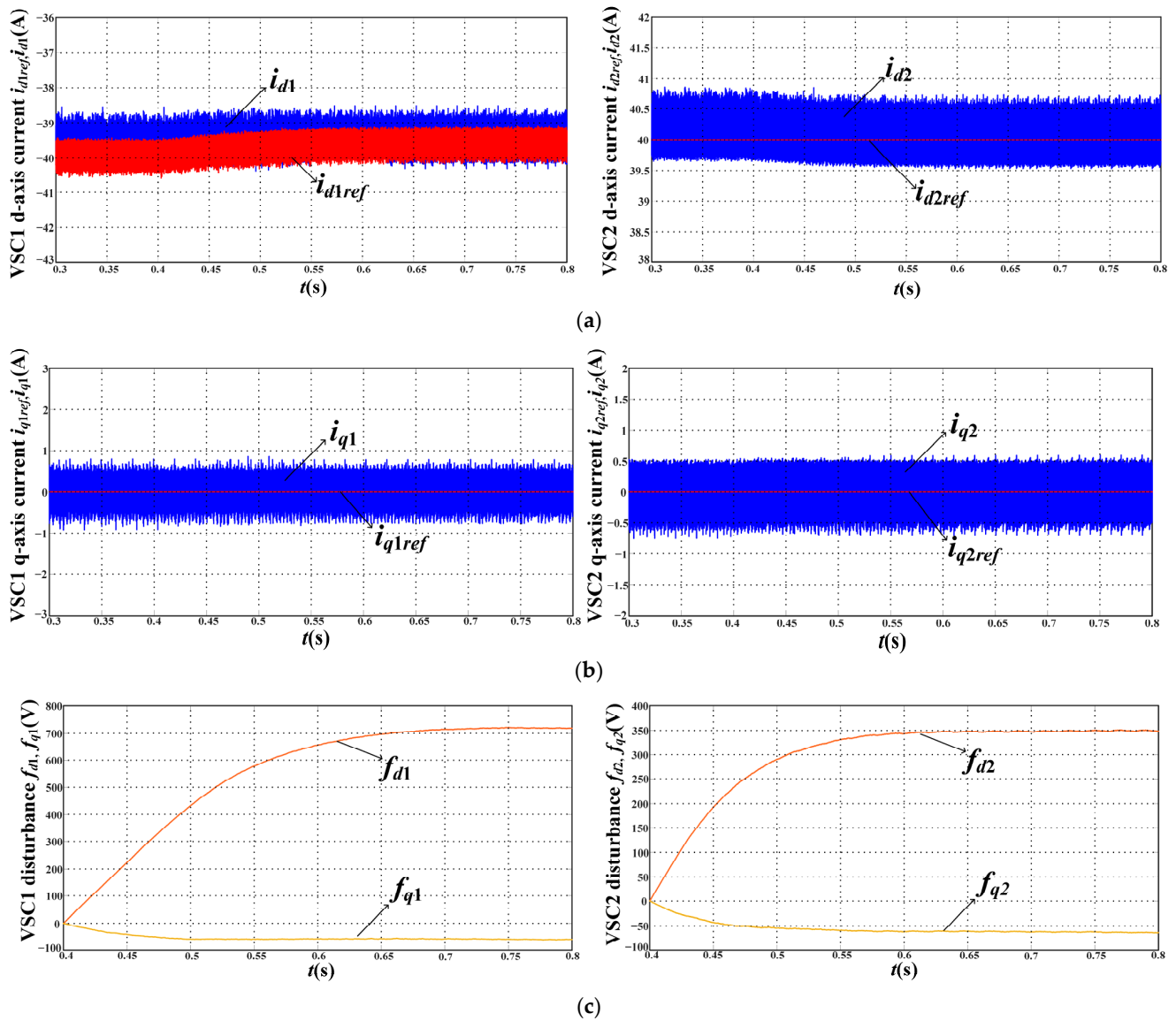
(a)

(b)

(c)

Figure 10. (**a**) *d*-axis currents of SOP with $0.3L_1$ and $0.3L_2$; (**b**) *q*-axis currents of SOP with $0.3L_1$ and $0.3L_2$; (**c**) disturbances observed by STO with $0.3L_1$ and $0.3L_2$.

Figure 11 shows the influences of resistance mismatches, when system resistances become $3R_1$ and $3R_2$, Figure 11a,b show the *d*-axis and *q*-axis currents of SOP system, it can be seen that resistance mismatches have less influence than inductance mismatches. As shown in Figure 11c, disturbances caused by resistance mismatches can be observed by STO. Therefore, it can be proved that the proposed STC and TV-MPC with STO can reduce the currents error obviously when parameter mismatches have occurred in the SOP system.
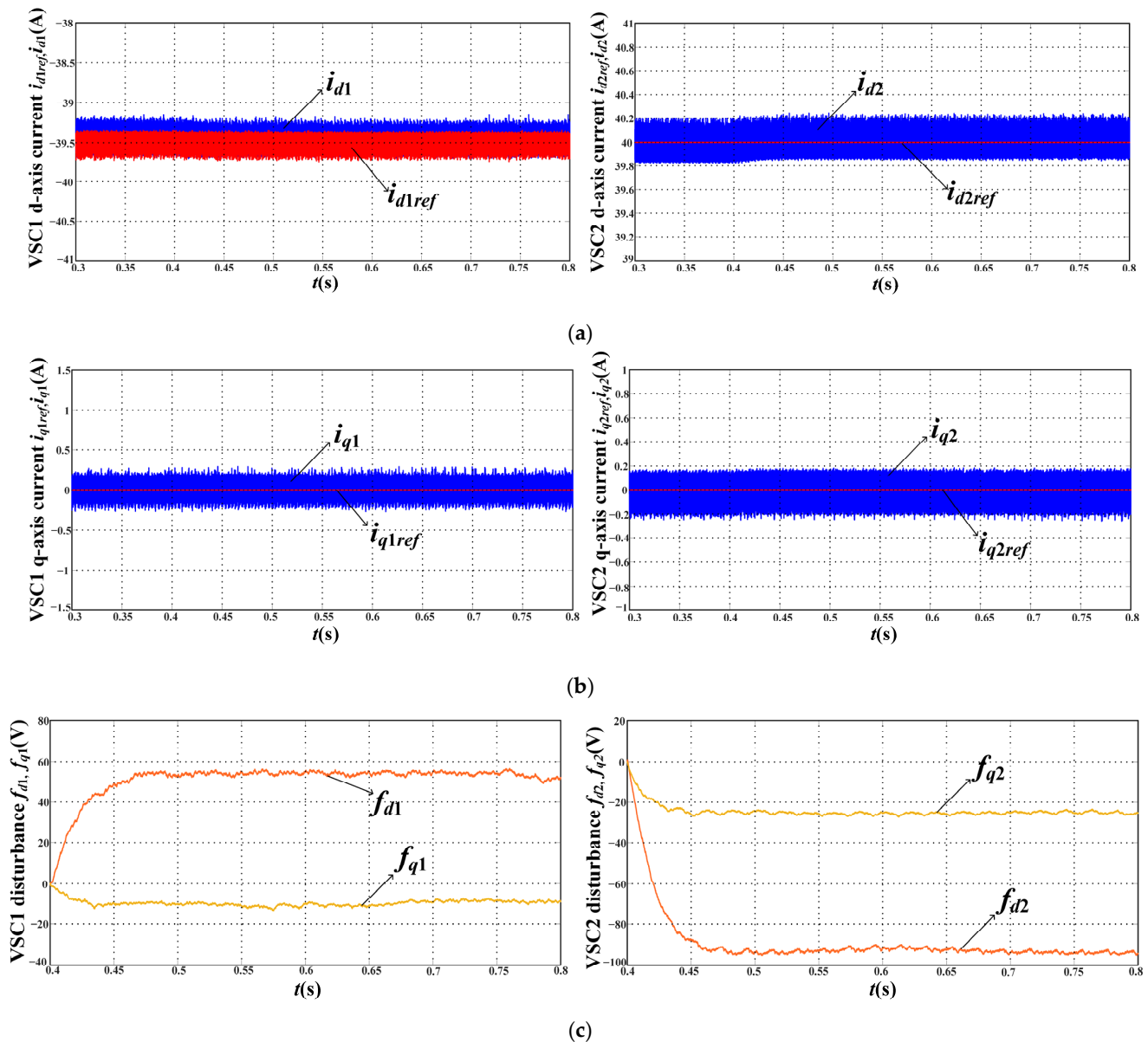
Figure 11. (**a**) *d*-axis currents of SOP with $3R_1$ and $3R_2$; (**b**) *q*-axis currents of SOP with $3R_1$ and $3R_2$; (**c**) disturbances observed by STO with $3R_1$ and $3R_2$.

7. Discussion

For the better performance of the SOP system, increasing the number of ports, considering the faults that may occur in the system, taking V*f* mode into consideration, and an experimental study of the SOP system will be the future work.

8. Conclusions

In this paper, a STC and TV-MPC with STO was proposed to improve the operation of the SOP system. Considering the disturbances caused by parameter mismatches and unmodelled dynamics, the STO was designed to observe the disturbances, and steady-state currents can track the reference currents correctly with the use of STO. In addition, aiming at the problems such as long start-up time, overshoot and poor robustness caused by traditional out-loop PI controller, an outer-loop STC was designed to improve the performance of the DC-side voltage. Moreover, in order to reduce the current harmonics, an inner-loop TV-MPC method was proposed. The simulation results show that STC and TV-MPC with STO can reduce current harmonics effectively while the DC voltage has a

better operation state, when parameter mismatches have occurred in the SOP system, STO can observe the disturbances correctly, which prove the effectiveness and correctness of the proposed method.

Author Contributions: Z.W.: conceptualization, algorithm innovation, methodology, and writing—original draft; H.Z.: data and formal analysis, investigation, software, simulation, and writing—original draft; H.S.: formal analysis, and writing—review and editing; All authors have read and agreed to the published version of the manuscript.

Institutional Review Board Statement: Not applicable.

Informed Consent Statement: Not applicable.

Data Availability Statement: Not applicable.

Conflicts of Interest: The authors declare no conflict of interest.

References

1. Bahrami, S.; Amini, M.H.; Shafie-Khah, M.; Catalão, J.P.S. A Decentralized Renewable Generation Management and Demand Response in Power Distribution Networks. *IEEE Trans. Sustain. Energy* **2018**, *4*, 1783–1797. [CrossRef]
2. Wang, C.; Song, G.; Li, P.; Ji, H.; Zhao, J.; Wu, J. Optimal siting and sizing of soft open points in active electrical distribution networks. *Appl. Energy* **2017**, *189*, 301–309. [CrossRef]
3. Jiang, X.; Zhou, Y.; Ming, W.; Yang, P.; Wu, J. An Overview of Soft Open Points in Electricity Distribution Networks. *IEEE Trans. Smart Grid* **2022**, *13*, 1899–1910. [CrossRef]
4. Wu, R.; Ran, L.; Weiss, G.; Yu, J. Control of a synchronverter-based soft open point in a distribution network. *J. Eng.* **2019**, *16*, 720–727. [CrossRef]
5. Cao, W.; Wu, J.; Jenkins, N.; Wang, C.; Green, T. Operating principle of Soft Open Points for electrical distribution network operation. *Appl. Energy* **2016**, *164*, 245–257. [CrossRef]
6. Cai, Y.; Qu, Z.; Yang, H.; Zhao, R.; Lu, Y.; Yang, Y. Research on an Improved Droop Control Strategy for Soft Open Point. In Proceedings of the 2018 21st International Conference on Electrical Machines and Systems (ICEMS), Jeju, Korea, 7–10 October 2018; pp. 2000–2005.
7. Falkowski, P.; Sikorski, A. Finite Control Set Model Predictive Control for Grid-Connected AC–DC Converters with LCL Filter. *IEEE Trans. Ind. Electron.* **2018**, *4*, 2844–2852. [CrossRef]
8. Zhang, X.; Wu, X.; Tan, G.; Zhang, W.; Wang, Q. A Dual-Vector Model Predictive Control Method with Minimum Current THD. *IEEE Trans. Power Electron.* **2021**, *9*, 9758–9762. [CrossRef]
9. Li, H.; Lin, M.; Yin, M.; Ai, J.; Le, W. Three-Vector-Based Low-Complexity Model Predictive Direct Power Control Strategy for PWM Rectifier Without Voltage Sensors. *IEEE J. Emerg. Sel. Top. Power Electron.* **2019**, *1*, 240–251. [CrossRef]
10. Zhan, S.; Na, J.; Li, G.; Wang, B. Adaptive Model Predictive Control of Wave Energy Converters. *IEEE Trans. Sustain. Energy* **2020**, *1*, 229–238. [CrossRef]
11. Liu, X.; Wang, D.; Peng, Z. Cascade-Free Fuzzy Finite-Control-Set Model Predictive Control for Nested Neutral Point-Clamped Converters with Low Switching Frequency. *IEEE Trans. Control Syst. Technol.* **2019**, *5*, 2237–2244. [CrossRef]
12. Xue, C.; Song, W.; Wu, X.; Feng, X. A Constant Switching Frequency Finite-Control-Set Predictive Current Control Scheme of a Five-Phase Inverter with Duty-Ratio Optimization. *IEEE Trans. Power Electron.* **2018**, *4*, 3583–3594. [CrossRef]
13. Cortes, P.; Rodriguez, J.; Silva, C.; Flores, A. Delay compensation in model predictive current control of a three-phase inverter. *IEEE Trans. Ind. Electron.* **2011**, *2*, 1323–1325. [CrossRef]
14. Jin, T.; Shen, X.; Su, T.; Flesch, R.C.C. Model Predictive Voltage Control Based on Finite Control Set with Computation Time Delay Compensation for PV Systems. *IEEE Trans. Energy Convers.* **2019**, *1*, 330–338. [CrossRef]
15. Young, H.A.; Perez, M.A.; Rodriguez, J. Analysis of Finite-Control-Set Model Predictive Current Control with Model Parameter Mismatch in a Three-Phase Inverter. *IEEE Trans. Ind. Electron.* **2016**, *5*, 3100–3107. [CrossRef]
16. Zhang, X.; Zhang, L.; Zhang, Y. Model Predictive Current Control for PMSM Drives with Parameter Robustness Improvement. *in IEEE Trans. Power Electron.* **2019**, *2*, 1645–1657. [CrossRef]
17. Siami, M.; Khaburi, D.A.; Rodríguez, J. Torque Ripple Reduction of Predictive Torque Control for PMSM Drives with Parameter Mismatch. *IEEE Trans. Power Electron.* **2017**, *9*, 7160–7168. [CrossRef]

18. Ghanes, M.; Trabelsi, M.; Abu-Rub, H.; Ben-Brahim, L. Robust Adaptive Observer-Based Model Predictive Control for Multilevel Flying Capacitors Inverter. *IEEE Trans. Ind. Electron.* **2016**, *12*, 7876–7886. [CrossRef]

19. Yang, R.; Wang, M.; Li, L.; Wang, G.; Zhong, C. Robust Predictive Current Control of PMLSM With Extended State Modeling Based Kalman Filter: For Time-Varying Disturbance Rejection. *IEEE Trans. Power Electron.* **2020**, *2*, 2208–2221. [CrossRef]

20. Yang, M.; Lang, X.; Long, J.; Xu, D. Flux Immunity Robust Predictive Current Control with Incremental Model and Extended State Observer for PMSM Drive. *IEEE Trans. Power Electron.* **2017**, *12*, 9267–9279. [CrossRef]

21. Zhao, Y.; Qiao, W.; Ha, D. A Sliding-Mode Duty-Ratio Controller for DC/DC Buck Converters with Constant Power Loads. *IEEE Trans. Ind. Appl.* **2014**, *2*, 1448–1458. [CrossRef]

22. Wang, C.; Mi, Y.; Fu, Y.; Wang, P. Frequency Control of an Isolated Micro-Grid Using Double Sliding Mode Controllers and Disturbance Observer. *IEEE Trans. Smart Grid* **2018**, *2*, 923–930. [CrossRef]

23. Yang, H.; Zhang, Y.; Liang, J.; Gao, J.; Walker, P.D.; Zhang, N. Sliding-Mode Observer Based Voltage-Sensorless Model Predictive Power Control of PWM Rectifier Under Unbalanced Grid Conditions. *IEEE Trans. Ind. Electron.* **2018**, *7*, 5550–5560. [CrossRef]

24. Xia, J.; Guo, Y.; Dai, B.; Zhang, X. Sensor Fault Diagnosis and System Reconfiguration Approach for an Electric Traction PWM Rectifier Based on Sliding Mode Observer. *IEEE Trans. Ind. Appl.* **2017**, *5*, 4768–4778. [CrossRef]

25. Sebaaly, F.; Vahedi, H.; Kanaan, H.Y.; Moubayed, N.; Al-Haddad, K. Sliding Mode Fixed Frequency Current Controller Design for Grid-Connected NPC Inverter. *IEEE J. Emerg. Sel. Top. Power Electron.* **2016**, *4*, 1397–1405. [CrossRef]

26. Li, X.; Luo, X.; Li, S.; Li, J.; Guan, X. Consensus of second-order nonlinear multi-agent systems via sliding mode observer and controller. *J. Syst. Eng. Electron.* **2017**, *4*, 756–765.

27. Sadeghi, R.; Madani, S.M.; Ataei, M.; Kashkooli, M.R.A.; Ademi, S. Super-Twisting Sliding Mode Direct Power Control of a Brushless Doubly Fed Induction Generator. *IEEE Trans. Ind. Electron.* **2018**, *11*, 9147–9156. [CrossRef]

28. Hou, Q.; Ding, S.; Yu, X. Composite Super-Twisting Sliding Mode Control Design for PMSM Speed Regulation Problem Based on a Novel Disturbance Observer. *IEEE Trans. Energy Convers.* **2021**, *4*, 2591–2599. [CrossRef]

29. Hou, Q.; Ding, S. GPIO Based Super-Twisting Sliding Mode Control for PMSM. *IEEE Trans. Circuits Syst. II Express Briefs* **2021**, *2*, 747–751. [CrossRef]

30. Cao, Y.; Fu, Z.; Zhang, M.; Huang, J. Extended-State-Observer-Based Super Twisting Control for Pneumatic Muscle Actuators. *Actuators* **2021**, *10*, 35. [CrossRef]

31. Liu, Y.-C.; Laghrouche, S.; Depernet, D.; Djerdir, A.; Cirrincione, M. Disturbance-Observer-Based Complementary Sliding-Mode Speed Control for PMSM Drives: A Super-Twisting Sliding-Mode Observer-Based Approach. *IEEE J. Emerg. Sel. Top. Power Electron.* **2021**, *9*, 5416–5428. [CrossRef]

32. Luo, W.; Vazquez, S.; Liu, J.; Gordillo, F.; Franquelo, L.G.; Wu, L. Control System Design of a Three-Phase Active Front End Using a Sliding-Mode Observer. *IEEE Trans. Syst. Man Cybern. Syst.* **2022**, *52*, 739–748. [CrossRef]

33. Fu, D.; Zhao, X.; Zhu, J. A Novel Robust Super-Twisting Nonsingular Terminal Sliding Mode Controller for Permanent Magnet Linear Synchronous Motors. *IEEE Trans. Power Electron.* **2022**, *3*, 2936–2945. [CrossRef]

34. Han, S.I. Fuzzy Supertwisting Dynamic Surface Control for MIMO Strict-Feedback Nonlinear Dynamic Systems with Supertwisting Nonlinear Disturbance Observer and a New Partial Tracking Error Constraint. *IEEE Trans. Fuzzy Syst.* **2019**, *11*, 2101–2114. [CrossRef]

35. Xu, Y.; Ding, X.; Wang, J.; Wang, C. Robust three-vector-based low-complexity model predictive current control with supertwisting-algorithm-based second-order sliding-mode observer for permanent magnet synchronous motor. *IET Power Electron.* **2019**, *11*, 2895–2903. [CrossRef]

36. Hur, N.; Jung, J.; Nam, K. A fast dynamic DC-link power-balancing scheme for a PWM converter-inverter system. *IEEE Trans. Ind. Electron.* **2001**, *48*, 794–803.

37. Rodriguez, J.; Pontt, J.; Silva, C.; Correa, P.; Lezana, P.; Cortes, P.; Ammann, U. Predictive Current Control of a Voltage Source Inverter. *IEEE Trans. Ind. Electron.* **2007**, *54*, 495–503. [CrossRef]

38. Guo, B.; Su, M.; Sun, Y.; Wang, H.; Dan, H.; Tang, Z.; Cheng, B. A Robust Second-Order Sliding Mode Control for Single-Phase Photovoltaic Grid-Connected Voltage Source Inverter. *IEEE Access* **2019**, *7*, 53202–53212. [CrossRef]

39. Moreno, J.A.; Osorio, M. Strict Lyapunov Functions for the Super-Twisting Algorithm. *IEEE Trans. Autom. Control* **2012**, *4*, 1035–1040. [CrossRef]